Biosensors and Bioelectronics 145 (2019) 111712

Contents lists available at ScienceDirect

Biosensors and Bioelectronics

journal homepage: www.elsevier.com/locate/bios

Dual-mode visible light-induced aptasensing platforms for bleomycin detection based on CdS–In_2S_3 heterojunction

Mengjun Sun, Yuhan Zhu, Kai Yan, Jingdong Zhang*

Key Laboratory of Material Chemistry for Energy Conversion and Storage (Ministry of Education), School of Chemistry and Chemical Engineering, Huazhong University of Science and Technology, Luoyu Road 1037, Wuhan, 430074, PR China

ARTICLE INFO

Keywords:
CdS–In_2S_3
Photoelectrochemical aptasensor
Self-powered aptasensor
Bleomycin

ABSTRACT

CdS–In_2S_3 heterojunction with enhanced photoelectrochemical (PEC) performance was synthesized to construct dual-mode visible light-induced biosensors for highly sensitive and selective detection of bleomycin (BLM). Due to improved absorption in the visible region and suppressed recombination of electron-hole pairs in the heterojunction, CdS–In_2S_3 composite exhibited enhanced photocurrent response under visible light illumination. Using CdS–In_2S_3 as photoactive materials and BLM-binding aptamer as recognition element, a PEC aptasensor displaying a declined photocurrent response to BLM was facilely constructed, which was linear to BLM concentration in the range of 5.0–250 nM. On the other hand, the CdS–In_2S_3 photoanode was employed to construct a photofuel cell (PFC). In such a PFC, the oxidation of water on CdS–In_2S_3 photoanode under visible light illumination and the reduction of oxygen on Pt cathode led to the generation of electricity. When BLM-binding aptamer was immobilized on CdS–In_2S_3 photoanode, the output power of the PFC was inversely proportional to the logarithm of BLM concentration from 10 to 250 nM, offering a visible light-induced self-powered sensing platform for BLM detection. Both of the proposed sensors showed high selectivity, good reproducibility and high stability. They were successfully applied to the determination of BLM in human serum samples.

1. Introduction

Bleomycin (BLM) is an antibiotic isolated from *Streptomyces verticillus* (Hay et al., 1991; Povirk and Finley Austin, 1991). Because of its advantages of low immunosuppression and myelosuppression, BLM has been widely utilized as chemotherapeutic agent against Hodgkin's disease, non-Hodgkin lymphoma, testicular cancer and malignant pleural effusion (Galm et al., 2005; Yu et al., 2013). It is believed that the antitumor activity of BLM derives from its ability through a sequence-selective, metal-dependent oxidative cleavage of DNA in the presence of oxygen. For instance, in the presence of Fe^{2+}, a binary complex (Fe^{2+}-BLM) forming between BLM and Fe^{2+} can activate molecular oxygen to produce free radicals which induce the cleavage of single- or double-stranded DNA (Akiyama et al., 2008). Nevertheless, inappropriate clinical utilization of BLM can cause some fatal side effects such as renal and lung toxicity, especially pulmonary fibrosis (Hay et al., 1991; Liu et al., 2008; Wang et al., 2017). Therefore, an assay of BLM in pharmaceuticals and clinical samples is of significant importance. As the most classical instrumental technique for pharmaceutical analysis, high-performance liquid chromatography (HPLC) has been established for quantitative determination of BLM (Malik et al., 2013). But HPLC is time-consuming, cost-expensive and need complicated separation procedures. Other instrumental techniques such as enzyme immunoassay (EIA) (Fujiwara et al., 1981), radioimmunoassay (RIA) (Teale et al., 1977), fluorescence resonance energy transfer (FRET) (Pei et al., 2016), fluorescence (Ma et al., 2009) and electrochemistry (Zhou et al., 2018) have also been developed for BLM detection. However, all these methods are based on the interaction between Fe^{2+}-BLM complex and DNA, which requires time-consuming procedure for the preparation of Fe^{2+}-BLM solution followed by mixing metallobleomycin with DNA to induce molecular change of DNA for detection.

In recent years, photoelectrochemical (PEC) sensors have been extensively developed for detection of various analytes including antibiotics (Zhu et al., 2019), biomarkers (Ge et al., 2016), proteins (Ma et al., 2016), cells (Qian et al., 2010), heavy metals (Han et al., 2013), and organic pollutants (Sun et al., 2019). Generally, PEC sensing can be facilely realized on the basis of traditional three-electrode cell coupled with photoirradiation; whereas its separate light source and electrochemical detection system can provide lower background and higher responsive signal than electrochemical sensing. Most of PEC sensors work in a “photocurrent” mode which is realized through the photogenerated electron transfer between photoelectrode and analyte. On the

* Corresponding author.
E-mail address: zhangjd@mail.hust.edu.cn (J. Zhang).

https://doi.org/10.1016/j.bios.2019.111712
Received 6 July 2019; Received in revised form 6 September 2019; Accepted 16 September 2019
Available online 18 September 2019
0956-5663/

other hand, the coupling of electrochemical detection with photoirradiation can also be achieved through a "self-powered sensing" mode based on photofuel cell (PFC). Different from three-electrode PEC sensing system, self-powered sensing only needs two electrodes. Moreover, it does not need external power supplies and complex devices, and thus can provide a feasible approach to the construction of miniaturized, implantable or portable device (Çakıroğlu and Özacar, 2018; Wang et al., 2014). So far, PFCs that can generate fuel concentration-dependent output during the photocatalytic reactions (Chen et al., 2019) have been used to develop self-powered sensors for detection of glucose (Yan et al., 2016), kanamycin (Ji et al., 2019), gallic acid (Santos et al., 2018) and 3,3′,4,4′-tetrachlorobiphenyl (PCB77) (Yan et al., 2018).

Although the detection modes of PEC and PFC-based sensors are different, both of them need to use photoelectrode prepared with photoactive materials. Various semiconductors including metal oxides and metal sulphides have been employed as photoactive materials (Di et al., 2019; Liu et al., 2019; Shen et al., 2012). Among them, CdS has been one of the most widely used photocatalysts because of its relatively narrow band gap (2.4 eV) and high absorption activity in the visible region (Tsuji et al., 2004). However, the application of CdS suffers from the fast recombination of photogenerated carriers and photocorrosion. To improve the performance of CdS, coupling CdS with other semiconductors possessing appropriate band edges to form heterojunction structures such as CdS/TiO_2 (Liu et al., 2012; Low et al., 2019), CdS/C_3N_4 (Xu et al., 2018), CdS/Bi_2S_3 (Li et al., 2011) and CdS/MoS_2 (Zang et al., 2016) have been explored. On the other hand, β-In_2S_3 is also a sulphide semiconductor with band gap of 2.0–2.3 eV, which has been considering as a promising photoactive material under visible light irradiation. In particular, due to its favourable energy band position, stable chemical composition and low toxicity (Zhou et al., 2014), In_2S_3 has been widely applied to the preparation of composite photocatalysts such as In_2O_3@In_2S_3 (Li et al., 2014), In_2S_3/ZnO (Li et al., 2018), In_2S_3/g-C_3N_4 (Xing et al., 2014) and In_2S_3/TiO_2 (Han et al., 2016).

In the present work, we proposed iron-free aptasensing strategies for BLM detection under visible light illumination. Considering that the well-matched band edges of In_2S_3 and CdS were advantageous for charge separation and improving the photocatalytic activity, we prepared heterojunction of CdS–In_2S_3 to act as photoactive materials for constructing the sensors. The CdS–In_2S_3 composite was prepared by *in situ* formation of CdS nanoparticles on In_2S_3. Compared with pure CdS or In_2S_3, CdS–In_2S_3 exhibited obviously improved photocurrent response. When BLM-binding aptamer was immobilized on the CdS–In_2S_3 photoanode, a PEC aptasensor exhibited a declined photocurrent response to BLM was fabricated. On the other hand, the aptamer-immobilized CdS–In_2S_3 photoanode was employed to construct a PFC-based sensor. In the designed membraneless PFC, water was oxidized to oxygen by photocatalysis on photoanode while oxygen was reduced to water on Pt cathode, leading to the generation of electricity which could provide detection signal without using an external electrical power supply. When BLM was present in the solution, the output of PFC decreased owing to the formation of BLM-aptamer complex. Thus, novel dual-mode BLM sensing platforms under visible light illumination were constructed, as illustrated in Scheme 1.

2. Experimental

2.1. Chemicals and materials

BLM, oxytetracycline (OTC), tetracycline (TC), kanamycin (Kana), streptomycin (SRT), ampicillin (AMP), lysine (Lys), tryptophan (Trp), glucose (Glu) and poly (diallyldimethylammonium chloride) (PDDA, MW 100000–200,000, 20 wt% in H_2O) were obtained from Aladdin Reagent Co., Ltd. (Shanghai, China). Cadmium acetate dihydrate [$Cd(CH_3COO)_2{\cdot}2H_2O$] was purchased from Qiangshun Chemical Co., Ltd. (Jiangsu, China). All the other reagents of analytical grade were acquired from Sinopharm Chemical Reagent Co., Ltd. (Shanghai, China) and used without further purification. BLM-binding aptamer with a sequence of 5′-CGC TTT AAA AAA AGC G-3′ was provided by Sangon Biotech Co. Ltd. (Shanghai, China). Indium tin oxide (ITO) conducting glass was obtained from South China Science & Technology Co., Ltd. (Shenzhen, China). Deionized water was used throughout the investigation.

2.2. Synthesis of CdS–In_2S_3 heterojunction

In_2S_3 was synthesized via a solvothermal method. In a typical procedure, 0.23 g thioacetamide was added into 60 mL 0.02 mM $InCl_3{\cdot}4H_2O$ dissolved in deionized water under vigorous stirring, leading to the formation of a uniform solution. The mixture was transferred into a 100 mL Teflon-lined autoclave, further sealed in a stainless steel tank, and heated to 180 °C in an electric oven for 12 h. After the autoclave was naturally cooled down to room temperature, the sample was washed with deionized water and ethanol, respectively, and then dried at 60 °C in air.

CdS–In_2S_3 composite was also prepared via the hydrothermal method by *in situ* formation of CdS on In_2S_3. Firstly, In_2S_3 (120 mg) was re-dispersed in 30 mL of deionized water. After 0.5-h ultrasonication, $Cd(CH_3COO)_2{\cdot}2H_2O$ (0.32 g) and thioacetamide (0.18 g) was dissolved into the above solution and kept stirring for 1 h. Then, the mixture was transformed into a Teflon-lined stainless steel autoclave and allowed to react at 180 °C for 24 h. The autoclave was cooled to room temperature. The product was washed several times with deionized water and ethanol, respectively, and finally dried at 60 °C. The pure CdS was prepared similarly in the absence of In_2S_3.

2.3. Construction of sensors

Photoanode was fabricated by modifying ITO conducting glass with CdS–In_2S_3. Prior to modification, ITO glass (0.8 cm × 1.2 cm) was cleaned by successive sonication in acetone, mixed solution of ethanol and 2 M NaOH (v/v, 1:1), and deionized water for 20 min, respectively. After being dried with nitrogen gas, the ITO glass with an exposed geometric area of 0.096 cm^2 was coated with 8 μL of 3 mg/mL CdS–In_2S_3 suspension. The obtained CdS–In_2S_3/ITO electrode was dried at 60 °C in an oven. The modified electrode was treated with 2% PDDA solution containing 0.5 M NaCl to make the surface positively charged, followed by rinsing with distilled water to remove loosely adsorbed PDDA. Then, the electrode was incubated with 6 μL aptamer solution at 40 °C for 2 h to immobilize negatively charged aptamer via electrostatic attraction. After carefully rinsing with deionized water, the fabricated aptamer/CdS–In_2S_3/ITO electrode was stored in refrigerator for further use. When studying the performance of the sensor, the aptamer/CdS–In_2S_3/ITO electrode was incubated with desired concentration of BLM at 40 °C for 2.0 h, followed by thoroughly rinsing with deionized water.

2.4. Apparatus and procedure

The scanning electron microscopic (SEM) images and energy dispersive X-ray spectroscopic (EDS) mapping images were obtained on a Nova NanoSEM 450 instrument (FEI, Netherlands) equipped with IE250X-Max50 EDS (Oxford, UK). Transmission electron microscopic (TEM) analysis was carried out on a Tecnai G2 F30 TEM instrument (FEI, The Netherlands). The X-ray diffraction (XRD) patterns were recorded on a Bruker D8 Advance X-ray diffractometer (Bruker Instruments, Darmstadt, Germany) operating at 40 kV accelerating voltage and applied current of 40 mA with Cu K_α radiation. The UV–visible absorption spectra were measured with a TU-1900 UV–visible spectrometer (Beijing Purkinje General Instrument Company, China).

All electrochemical measurements in a quartz cell were performed

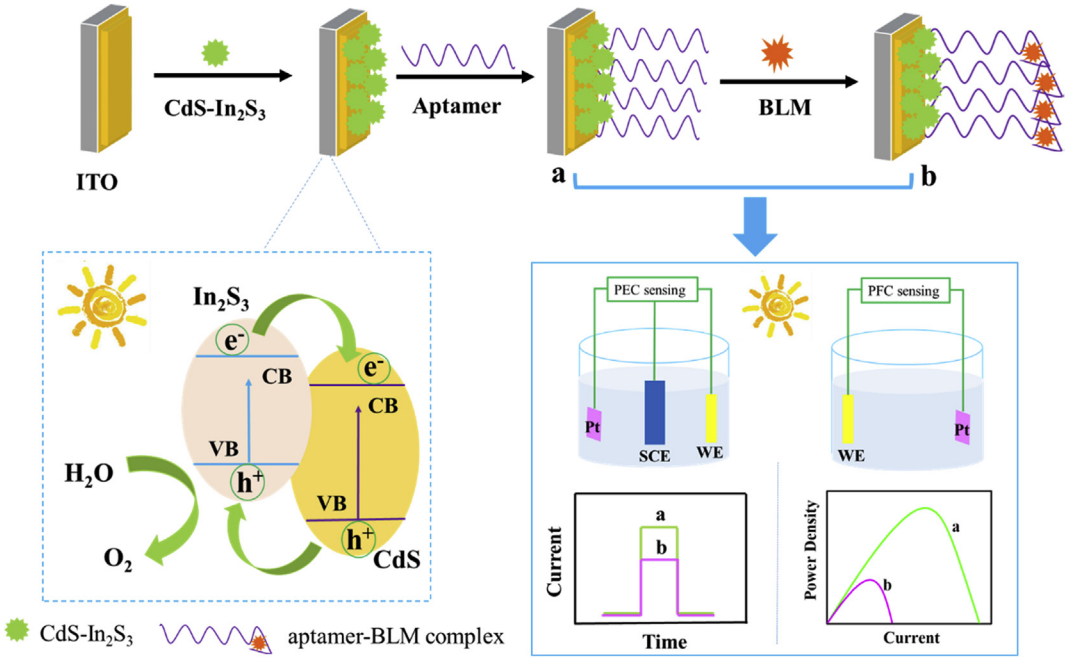

Scheme 1. Schematic illustration of the dual-mode aptasensing platforms for BLM detection based on CdS–In_2S_3 heterojunction.

on a CHI660A electrochemical working station (Shanghai Chenhua Instrument Co. Ltd., China). A CEL-S500/350 xenon lamp (CEAULIGHT Co., China) with an optical filter ($\lambda > 420$ nm) was used as the visible light source and the distance between the lamp and the photoanode surface was 10 cm. The PEC measurement was carried out in a conventional three-electrode system consisting of a photoanode working electrode, a saturated calomel reference electrode (SCE) and a Pt counter electrode. In PEC sensing, the photocurrent was recorded in 0.1 M phosphate buffer solution (PBS, pH 7.4) at the bias potential of 0.2 V via an on-off cycle of intermittent visible light irradiation. On the other hand, the PFC was comprised of a photoanode and Pt cathode in a quartz cell containing 0.1 M PBS (pH 7.4). The dependence of output cell voltage on current (*V–I* curve) of the PFC was obtained with galvanostatic polarization technique. The output power density (*P–I*) curve was obtained by plotting the power density ($V \times I/A$) vs. the current, where *A* was the geometric area of the photoanode.

3. Results and discussion

3.1. Materials characterization

The obtained CdS, In_2S_3 and CdS–In_2S_3 samples were characterized by SEM. As shown in Fig. 1A, many CdS nanoparticles in the diameter of 30–50 nm were observed. For In_2S_3, there appeared many dandelion-like porous microspheres with an average size of *ca.* 1.5 μm (Fig. 1B). When CdS and In_2S_3 formed composite, the dandelion-shape of In_2S_3 collapsed and the size of microspheres increased. Further observation showed that many aggregated CdS nanoparticles were loaded on the surface of In_2S_3 microspheres (Fig. 1C). Meanwhile, the elemental mapping results confirmed the existence and homogeneous distribution of Cd, In and S elements in the CdS–In_2S_3 composite (Fig. S1). The EDS elemental analysis (Fig. 1D) indicated that the atomic percentages of Cd, In and S in the composite were 24.61%, 22.17% and 52.61%, respectively, consistent with the stoichiometric proportion of CdS and In_2S_3. Moreover, In_2S_3 microspheres and CdS nanoparticles could also be seen in the composite sample by TEM observation (Fig. S2). The high-resolution transmission electron microscopic (HRTEM) image of the composite sample (Fig. 1E) revealed the lattice spacings of 0.323 nm and 0.193 nm, corresponding to the (311) and (440) planes of In_2S_3 (Chen et al., 2008), respectively. Besides, the lattice spacing of 0.207 nm corresponding to the (110) plane of CdS (Dai et al., 2014) was found, showing the formation of CdS–In_2S_3 heterojunction structure.

On the other hand, the crystalline nature of various materials was analyzed by XRD. As shown in curve a of Fig. 1F, the diffraction peaks at 26.5°, 44.0°, 52.1°, 54.6°, 70.4° and 72.8° were attributed to the (111), (220), (311), (222), (331) and (420) crystal planes of CdS, in agreement with cubic phase of CdS (JCPDS card no. 10-0454) (Dai et al., 2014). For the sample of In_2S_3 (curve b of Fig. 1F), all the diffraction peaks were readily indexed to the cubic phase of β-In_2S_3 (JCPDS card no. 032-0456) (Li et al., 2018). In the XRD pattern of CdS–In_2S_3 (curve c of Fig. 1F), all the diffraction peaks of In_2S_3 were clearly exhibited but few weak peaks of CdS were seen. This is due to the relatively stronger intensities of diffraction peaks of In_2S_3 than those of CdS.

3.2. Optical, impedance and photocurrent analysis

The optical absorption properties of the as-prepared materials were investigated by UV–Vis absorption spectroscopy. As depicted in Fig. 2A, CdS and In_2S_3 showed different absorption properties. The former exhibited relatively stronger absorption in the visible region while the latter showed relatively stronger absorption in the UV region. When CdS and In_2S_3 formed composite, enhanced absorption from UV to visible region was clearly observed, which was assigned to the fact that CdS could act as photosensitizer for trapping large numbers of photons from visible light (Sun et al., 2008).

The as-prepared materials were utilized to modify electrodes and the interfacial properties of modified electrodes were investigated by electrochemical impedance spectroscopy (EIS) using $[Fe(CN)_6]^{3-/4-}$ redox probe (Fig. S3). From the semicircle diameter of the Nyquist plots at high frequency region, the electron-transfer resistance (R_{et}) value of bare ITO was estimated to be 63.8 Ω. The R_{et} values of CdS/ITO, In_2S_3/ITO and CdS–In_2S_3/ITO increased to 136.6 Ω, 179.6 Ω and 158.8 Ω, respectively, owing to the low conductivity of these semiconducting materials. After aptamer was immobilized on the CdS–In_2S_3 electrode, the R_{et} value further increased to 244.1 Ω, ascribed to the electrostatic repulsion between negatively charged phosphate backbone of aptamer molecules and redox species of $[Fe(CN)_6]^{3-/4-}$. This result confirms the

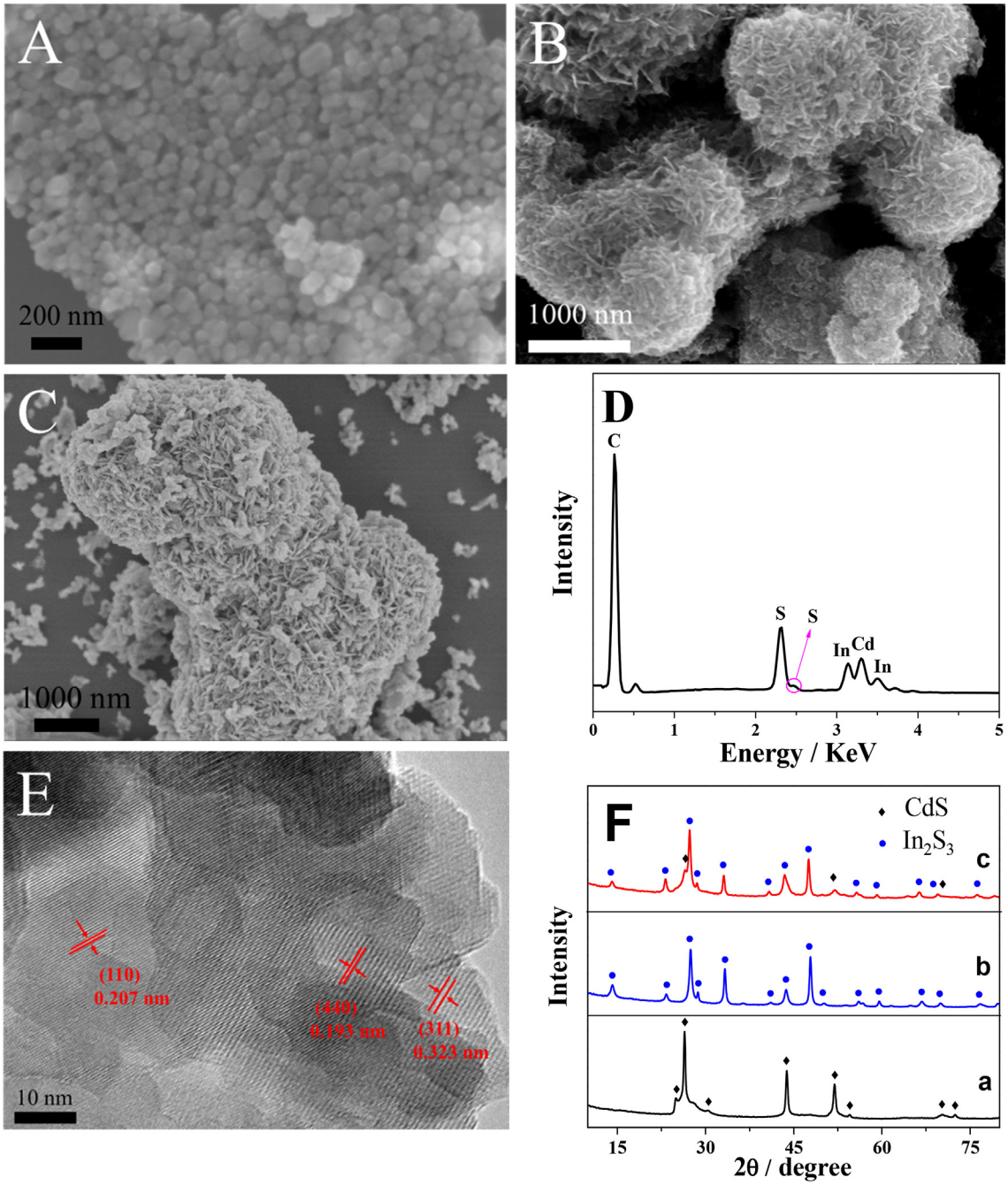

Fig. 1. SEM images of (A) CdS, (B) In_2S_3 and (C) CdS–In_2S_3. (D) EDS spectrum of CdS–In_2S_3. (E) HRTEM image of CdS–In_2S_3. (F) XRD patterns of (a) CdS, (b) In_2S_3 and (c) CdS–In_2S_3.

effective immobilization of aptamer on the electrode surface of CdS–In_2S_3/ITO.

Fig. 2B shows the photocurrent responses of various modified electrodes recorded in 0.1 M PBS (pH 7.4) under visible light illumination by applying a bias potential of 0.2 V. Among three modified electrodes, CdS–In_2S_3/ITO exhibited the highest anodic photocurrent, in accordance with the enhanced optical absorption ability of heterojunction. However, it was inconsistent with the fact that CdS–In_2S_3 has lower conductivity than CdS. The result implies that the optical absorption ability of semiconducting material affecting photocurrent response is more pronounced than its conductivity. Moreover, the formation of heterojunction is favourable for improving the photocurrent. Fig. 2C illustrates the transfer mechanism of photogenerated carriers on the CdS–In_2S_3 composite. From the energy band diagram, the conduction band (CB) of CdS is more positive than that of In_2S_3 while the valence band (VB) of In_2S_3 is more negative than that of CdS, thus forming an n-n heterojunction. Under visible light illumination, the photogenerated electrons at CB of In_2S_3 would quickly migrate to CB of CdS and fast transfer of the photogenerated holes from VB of CdS to VB of In_2S_3 occurs correspondingly. As a result, the recombination of electrons and holes is reduced and the photocurrent is enhanced.

Furthermore, the photocurrent responses CdS–In_2S_3/ITO before and after immobilizing aptamer for BLM capture were recorded at 0.2 V in 0.1 M PBS (pH 7.4) under visible light illumination. As shown in Fig. 2D, the photocurrent response of CdS–In_2S_3/ITO decreased slightly after incubation with BLM, due to adsorption of small amount of BLM on the electrode. After aptamer was immobilized on CdS–In_2S_3/ITO, the photocurrent decreased obviously, attributed to the steric hindrance of

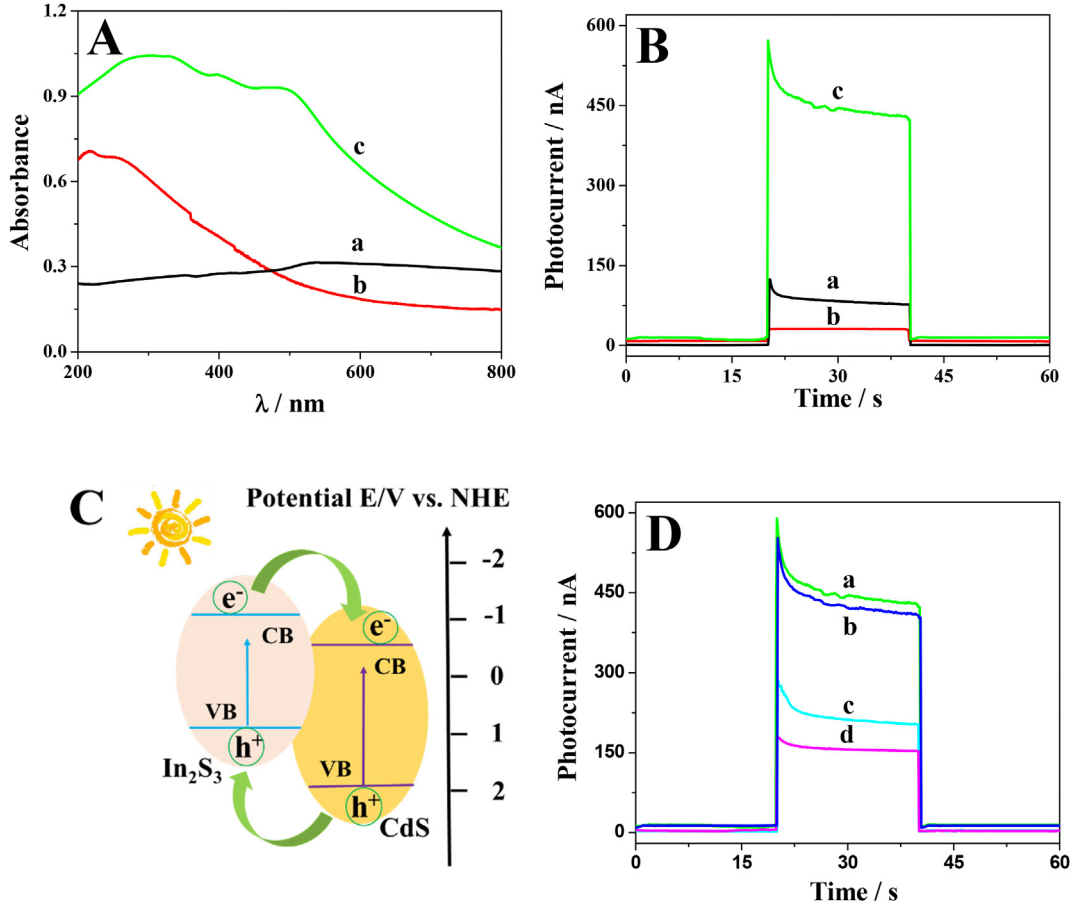

Fig. 2. (A) UV–Vis absorption spectra of (a) CdS, (b) In_2S_3 and (c) CdS–In_2S_3 heterojunction. (B) Photocurrent responses of (a) CdS/ITO, (b) In_2S_3/ITO and (c) CdS–In_2S_3/ITO recorded in 0.1 M PBS (pH 7.4) at +0.2 V. (C) Energy band diagram of CdS–In_2S_3 heterojunction. (D) Photocurrent responses recorded in 0.1 M PBS (pH 7.4) at +0.2 V on different modified electrodes: (a) CdS–In_2S_3/ITO, (b) CdS–In_2S_3/ITO incubated with 100 nM BLM, (c) aptamer/CdS–In_2S_3/ITO and (d) aptamer/CdS–In_2S_3/ITO incubated with 100 nM BLM.

aptamer for electron transfer between the electrode and electron donor (Okoth et al., 2018; Tabrizi et al., 2017). While aptamer/CdS–In_2S_3/ITO was incubated with BLM, the photocurrent response was further decreased. This can be attributed to enhanced steric hindrance of aptamer-BLM complex for electron transfer by captured BLM as an insulating organic molecule (Dong et al., 2017; Zhu et al., 2016). Accordingly, the proposed aptamer/CdS–In_2S_3/ITO electrode could be utilized as a visible light PEC sensor for BLM.

3.3. PEC sensing of BLM

The influences of CdS–In_2S_3 concentration (Fig. S4), applied potential (Fig. S5) and aptamer concentration (Fig. S6) on the photocurrent responses of aptamer/CdS–In_2S_3/ITO were investigated in 0.1 M PBS (pH 7.4). The photocurrent difference (ΔPI) before and after incubation with BLM was evaluated to quantitatively compare the response of the sensor to BLM. The results indicated that 3 g/L CdS–In_2S_3, +0.2 V bias potential and 1.0 μM aptamer exhibited the best photocurrent response to BLM. Therefor, under such optimum conditions, the fabricated aptamer/CdS–In_2S_3/ITO was employed for PEC sensing of BLM. Fig. 3A depicts the photocurrent responses of aptamer/CdS–In_2S_3/ITO toward BLM at different concentrations. The photocurrent was found to decrease linearly with the increase of BLM concentration from 5.0 to 250 nM. The linear regression equation could be expressed as ΔPI/nA = 0.407C/nM + 14.41 (correlation coefficient R^2 = 0.999). The sensitivity of this PEC sensor was 4.24 A M^{-1} cm^{-2}. The detection limit (3S/N) was estimated to be 0.85 nM, which was superior to many previously reported BLM sensors (Table S1). Although an electrochemical DNA sensor (Yin et al., 2010) showed wider linear range and lower detection limit than this PEC sensor, it strongly depended on the interaction between DNA and Fe^{2+}-BLM and required time-consuming procedures. By contrast, our proposed iron-free strategy is simple, fast and cost-effective for BLM detection.

The reproducibility of the developed sensor was evaluated by checking the responses of ten independently prepared aptamer/CdS–In_2S_3/ITO electrodes toward 100 nM BLM. A relative standard deviation (RSD) value of 4.2% was obtained, showing good reproducibility. On the other hand, the interference studies were carried out to evaluate the selectivity of the sensor. As shown in Fig. 3B, all of these tested compounds did not cause significant interference in the determination of BLM when equal amount of different interferents were added into 100 nM BLM solution, indicating high selectivity of the proposed PEC aptasensor for BLM detection, due to the specific interaction between BLM and aptamer. Moreover, the stability of the proposed aptasensor was also investigated. The fabricated aptamer/CdS–In_2S_3/ITO retained 98.8% of its original photocurrent response toward 100 nM BLM after the electrode was stored at 4 °C in a refrigerator for two weeks, indicating good stability.

3.4. Construction of PFC for self-powered sensing of BLM

On the other hand, CdS–In_2S_3/ITO was explored to construct a two-electrode PFC for self-powered sensing of BLM. Before constructing PFC, the polarization curves of both electrodes were investigated to evaluate the feasibility of the PFC. As shown in Fig. 4A, on CdS–In_2S_3/ITO electrode, no anodic current was observed in the dark (curve a in

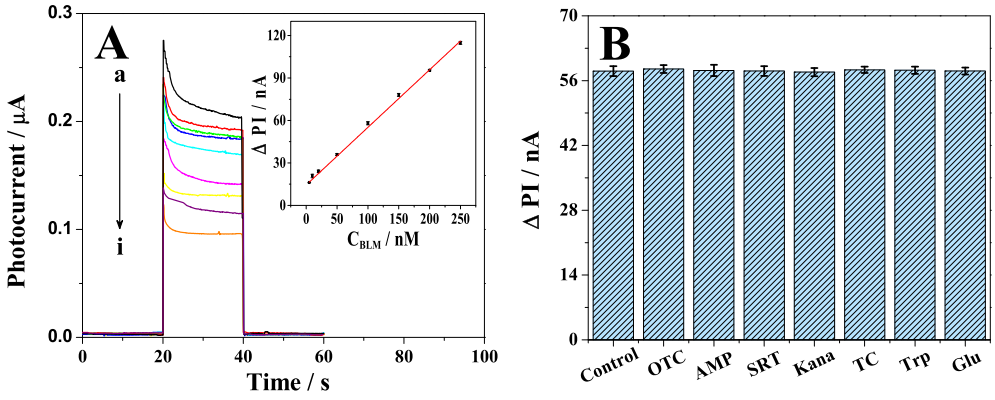

Fig. 3. (A) Photocurrent responses of the fabricated aptasensor in 0.1 M PBS (pH 7.4) after incubation with different concentrations of BLM: (a) 0, (b) 5, (c) 10, (d) 20, (e) 50, (f) 100, (g) 150, (h) 200 and (i) 250 nM. Inset: calibration curve for BLM on the PEC sensor. (B) Histogram for ΔPI obtained on PEC sensor incubated with 100 nM BLM solution containing equal amount of different interferants: OTC, TC, Kana, SRT, Lys, AMP, Trp and Glu. Error bars are derived from the standard deviation of three measurements.

Fig. 4A) while the onset potential for H_2O oxidation was −0.2 V (vs. SCE) under visible light illumination (curve b in Fig. 4A). Meanwhile, on Pt cathode (curve b in Fig. 4B), no reduction peak was observable in N_2-saturated electrolyte; whereas a strong reduction peak appeared in air-saturated electrolyte, due to the reduction of dissolved oxygen. The reduction of oxygen on Pt cathode started at 0.18 V (vs. SCE), higher than the onset potential for H_2O oxidation on CdS–In_2S_3/ITO photoanode, indicating the thermodynamic feasibility of the proposed H_2O–O_2 PFC without the introduction of additional mediator.

The performances of PFC constructed with a Pt cathode and different photoanodes were compared by recording the output voltage-current (*V–I*) curves and power density-current (*P–I*) curves, as illustrated in Fig. 4C and D. Compared with CdS/ITO and In_2S_3/ITO based PFC, the CdS–In_2S_3 photoanode based PFC showed larger open circuit potential (OCP) and higher maximum power density (P_{Max}). This result is consistent with the aforementioned enhanced PEC performance of CdS–In_2S_3 photoanode.

Considering that the output of fuel cell could directly provide the electrical signal responding to analyte concentration with no requirement of external power source, the CdS–In_2S_3 based PFC was explored for self-powered sensing of BLM. To realize the specific recognition of analyte, BLM-binding aptamer was immobilized on the CdS–In_2S_3/ITO photoanode. The results indicated that the OCP of the PFC reduced to 0.65 V (curve a in Fig. 5A) and the P_{Max} of the PFC decreased to 2.21 μW·cm^{-2} (curve a in Fig. 5B) when aptamer/CdS–In_2S_3/ITO was employed as the photoanode instead of CdS–In_2S_3/ITO, owing to the blocking effect of aptamer. After aptamer/CdS–In_2S_3/ITO was incubated with 100 nM BLM, the P_{Max} of PFC was further decreased to

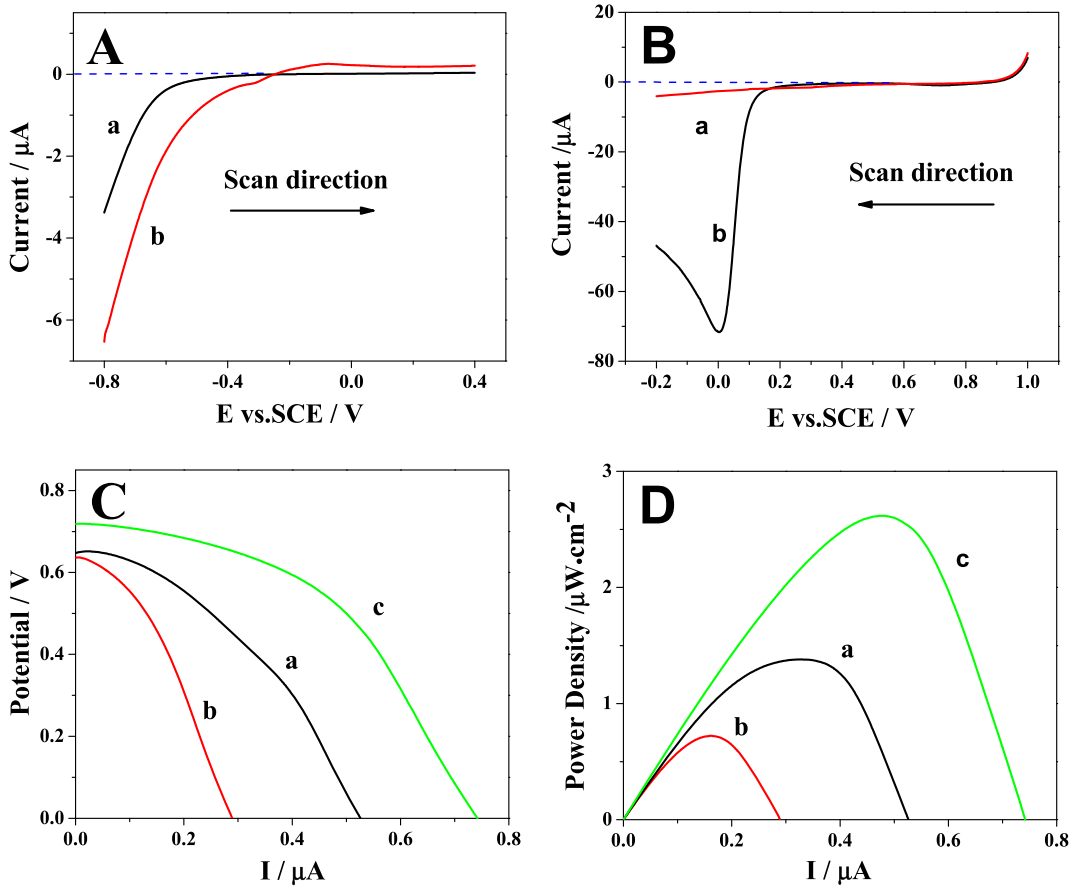

Fig. 4. (A) Polarization curves of CdS–In_2S_3/ITO photoanode (a) in the dark and (b) under photoirradiation in 0.1 M PBS (pH 7.4) at 2 mV/s. (B) Polarization curves of Pt cathode in 0.1 M PBS (pH 7.4) saturated with (a) N_2 and (b) air at 2 mV/s (C) *V–I* curves and (D) *P–I* curves of PFCs constructed with Pt cathode and different photoanodes: (a) CdS/ITO, (b) In_2S_3/ITO and (c) CdS–In_2S_3/ITO. The measurements of PFC were carried out in 0.1M PBS (pH 7.4) under visible light irradiation.

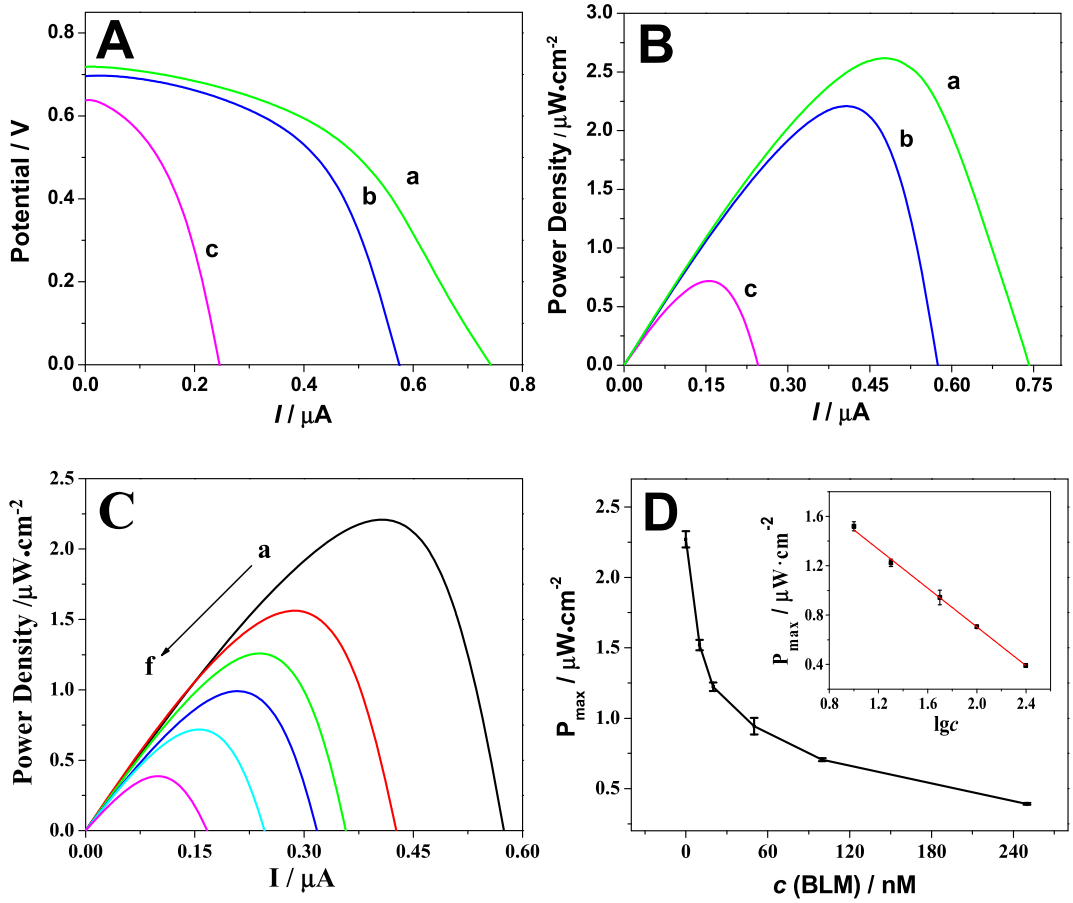

Fig. 5. (A) *V–I* curves and (B) *P–I* curves of PFCs constructed with (a) CdS–In_2S_3/ITO, (b) aptamer/CdS–In_2S_3/ITO and (c) aptamer/CdS–In_2S_3/ITO incubated with 100 nM BLM. (C) *P–I* curves of the proposed PFC incubated with BLM at different concentrations: (a) 0, (b) 10, (c) 20, (d) 50, (e) 100, (f) 200 nM. (D) Variation of P_{Max} values of the proposed self-powered aptasensor with BLM concentration. Inset: calibration curve for BLM detection by the proposed sensor. The measurements of PFC were carried out in 0.1M PBS (pH 7.4) under visible light irradiation. Error bars are derived from the standard deviation of three measurements.

0.71 μW·cm^{-2}, attributed to the formation of BLM-aptamer complex which could impede the diffusion of electron donor toward electrode surface to consume photogenerated holes. Accordingly, a visible light-induced self-powered sensing platform for BLM could be realized using the P_{Max} of PFC as detection signal. Fig. 5C shows the decrease of P_{Max} of PFC with increasing the concentration of BLM. The P_{Max} was found to be declined linearly with the logarithm of BLM concentration from 10 to 250 nM (Fig. 5D). The linear regression equation was expressed as P_{Max}/μW·cm^{-2} = −0.786 lgC/nM + 2.277 (R^2 = 0.998), with a detection limit (3S/N) of 1.0 nM. As listed in Table S1, although the LOD of such a self-powered sensing mode is slightly higher than the PEC sensing mode, it is still lower than many previously reported BLM sensors (Table S1).

The selectivity of the self-powered sensor was also evaluated by testing the output of the PFC toward 100 nM BLM in the presence of equal amount of different interferents. As displayed in Fig. S7, there was no significant change on the P_{Max} of the PFC after the addition of these compounds, suggesting the excellent selectivity of the fabricated detection system. Additionally, we also investigated the tolerance limit of these interferents for detection of 100 nM BLM on both developed sensors. The maximum molar ratio of interferent to BLM was determined when the responsive signal change in the absence and presence of interferent was no more than ± 5%. As shown in Table S2, the maximum molar ratios of these interferents to BLM reached 10 or 20, confirming that both sensors had good anti-interference ability.

The reproducibility of the proposed self-powered sensor was tested by carrying out ten independent experiments toward 100 nM BLM. The RSD of 1.8% showed the desirable reproducibility of the proposed method. Moreover, the stability of the sensor was assessed by checking the P_{Max} of PFC toward 100 nM BLM. The sensor still retained 97.5% of its original P_{Max} response after 10-day storage at 4 °C, showing acceptable stability.

3.5. Application to BLM detection in human serum

The feasibility of the proposed aptasensing strategies was studied for BLM detection in human serum with standard addition method. The human serum sample was provided by Hospital of Huazhong University of Science and Technology. Before measurement, the human serum sample was diluted with deionized water for 50 times and filtered with 0.22 μm nylon membrane filters. Then, the diluted serum sample was spiked with different concentrations of BLM. Table S3 summarizes the analytical results for the spiked serum samples using the proposed PEC aptasensor. As can be seen, the recovery values are in the range from 98.6% to 102.3%, showing the accuracy of the developed PEC aptasensor. Moreover, Table S4 summarizes the analytical results of spiked human serum samples using the PFC-based self-powered aptasensor. The recovery values in the range of 97.5%–102.4% suggest that the PFC-based sensor is also feasible for BLM determination in human serum sample.

4. Conclusions

In this work, we proposed dual-mode visible light-induced sensing platforms for BLM detection by using CdS–In_2S_3 heterojunction as photoactive material and BLM-binding aptamer as biorecognition

element. When BLM was present in the solution, the formation of aptamer-BLM complex resulted in decrease in photocurrent of PEC sensor or output power of PFC-based sensor. Both of the proposed sensors exhibited high selectivity, desirable reproducibility, and good stability. Our work not only offers new approaches to iron-free detection of BLM, but also demonstrates the perspective of CdS–In_2S_3 heterojunction for the development of visible light-induced sensors. Nevertheless, compared with previously reported electrochemical DNA sensor for BLM detection, the proposed iron-free aptasensors exhibited higher detection limit and narrower linear range. Therefore, coupling signal amplification strategy with PEC or PFC-based sensor in our future work will be explored to promote the sensing performance.

CRediT authorship contribution statement

Mengjun Sun: Investigation, Data curation, Writing - original draft. **Yuhan Zhu:** Methodology, Writing - review & editing. **Kai Yan:** Methodology, Writing - review & editing. **Jingdong Zhang:** Supervision, Funding acquisition, Writing - review & editing.

Declaration of competing interest

The authors declare that they have no known competing financial interests or personal relationships that could have appeared to influence the work reported in this paper.

Acknowledgements

This work was supported by the National Natural Science Foundation of China (Grant No. 61571198) and the opening fund of Hubei Key Laboratory of Bioinorganic Chemistry & Materia Medica (Grant No. BCMM201902). The authors thank the Analytical and Testing Center of Huazhong University of Science and Technology for help in the characterization of materials.

Appendix A. Supplementary data

Supplementary data to this article can be found online at https://doi.org/10.1016/j.bios.2019.111712.

References

Akiyama, Y., Ma, Q., Edgar, E., Laikhter, A., Hecht, S.M., 2008. J. Am. Chem. Soc. 130, 9650–9651.
Çakıroğlu, B., Özacar, M., 2018. Biosens. Bioelectron. 119, 34–41.
Chen, L.Y., Zhang, Z.D., Wang, W.Z., 2008. J. Phys. Chem. C 112, 4117–4123.
Chen, Y., Ji, W., Yan, K., Gao, J., Zhang, J., 2019. Nano Energy 61, 173–193.
Dai, X., Xie, M., Meng, S., Fu, X., Chen, S., 2014. Appl. Catal. B Environ. 158–159, 382–390.
Di, T., Xu, Q., Ho, W., Tang, H., Xiang, Q., Yu, J., 2019. ChemCatChem 11, 1394–1411.
Dong, X.Y., Cao, J.T., Liu, Y.M., Ma, S.H., 2017. Biosens. Bioelectron. 91, 246–252.
Fujiwara, K., Yasuno, M., Kitagawa, T., 1981. Cancer Res. 41, 4121.
Galm, U., Hager, M.H., Van Lanen, S.G., Ju, J., Thorson, J.S., Shen, B., 2005. Chem. Rev. 105, 739–758.
Ge, L., Wang, W., Hou, T., Li, F., 2016. Biosens. Bioelectron. 77, 220–226.
Han, M., Yu, L., Chen, W., Wang, W., Jia, J., 2016. Appl. Surf. Sci. 369, 108–114.
Han, D.M., Ma, Z.Y., Zhao, W.W., Xu, J.J., Chen, H.Y., 2013. Electrochem. Commun. 35, 38–41.
Hay, J., Shahzadi, S., Laurent, G., 1991. Arch. Toxicol. 65, 81–94.
Ji, W., Yan, K., Chen, Y., Gao, J., Zhang, J., 2019. Sens. Actuators, B 292, 129–135.
Li, H., Chen, C., Huang, X., Leng, Y., Hou, M., Xiao, X., Bao, J., You, J., Zhang, W., Wang, Y., Song, J., Wang, Y., Liu, Q., Hope, G.A., 2014. J. Power Sources 247, 915–919.
Li, M., Tu, X., Su, Y., Lu, J., Hu, J., Cai, B., Zhou, Z., Yang, Z., Zhang, Y., 2018. Nanoscale 10, 1153–1161.
Li, X., Chen, J., Li, H., Li, J., Xu, Y., Liu, Y., Zhou, J., 2011. J. Nat. Gas Chem. 20, 413–417.
Liu, J., Liu, Z., Hu, X., Kong, L., Liu, S., 2008. Luminescence 23, 1–6.
Liu, S., Zhang, N., Tang, Z., Xu, Y., 2012. ACS Appl. Mater. Interfaces 4, 6378–6385.
Liu, Y., Liu, M., Yin, D., Zhu, D., Swihart, M.T., 2019. Nanoscale 11, 136–144.
Low, J., Dai, B., Tong, T., Jiang, C., Yu, J., 2019. Adv. Mater. 31, 1802981–1802985.
Ma, Q., Akiyama, Y., Xu, Z., Konishi, K., Hecht, S.M., 2009. J. Am. Chem. Soc. 131, 2013–2022.
Ma, Z.Y., Ruan, Y.F., Xu, F., Zhao, W.W., Xu, J.J., Chen, H.Y., 2016. Anal. Chem. 88, 3864–3871.
Malik, M.Z., Ahmad, M., Muhammad, S., 2013. J. Chil. Chem. Soc. 58, 1674–1677.
Okoth, O.K., Yan, K., Feng, J., Zhang, J., 2018. Sens. Actuators, B 256, 334–341.
Pei, H., Zheng, Y., Kong, R., Xia, L., Qu, F., 2016. Biosens. Bioelectron. 85, 76–82.
Povirk, L.F., Finley Austin, M.J., 1991. Mutat. Res. 257, 127–143.
Qian, Z., Bai, H.J., Wang, G.L., Xu, J.J., Chen, H.Y., 2010. Biosens. Bioelectron. 25, 2045–2050.
Santos, G.K.C., Silva, F.G.S., Yotsumoto Neto, S., Santos, W.T.P., Luz, R.C.S., Damos, F.S., 2018. Electroanalysis 30, 1750–1756.
Shen, Z., Chen, G., Wang, Q., Yu, Y., Zhou, C., Wang, Y., 2012. Nanoscale 4, 2010–2017.
Sun, M., Li, R., Zhang, J., Yan, K., Liu, M., 2019. Nanoscale 11, 5982–5988.
Sun, W.T., Yu, Y., Pan, H.Y., Gao, X.F., Chen, Q., Peng, L.M., 2008. J. Am. Chem. Soc. 130, 1124–1125.
Tabrizi, M.A., Shamsipur, M., Saber, R., Sarkar, S., Ebrahimi, V., 2017. Biosens. Bioelectron. 98, 113–118.
Teale, J.D., Clough, J.M., Marks, V., 1977. Br. J. Canc. 35, 822–827.
Tsuji, I., Kato, H., Kobayashi, H., Kudo, H., 2004. J. Am. Chem. Soc. 126, 13406–13413.
Wang, H., Jiang, W., Li, W., Wang, L., 2017. Sens. Actuators, B 238, 318–324.
Wang, Y., Ge, L., Wang, P., Yan, M., Yu, J., Ge, S., 2014. Chem. Commun. 50, 1947–1949.
Xing, C., Wu, Z., Jiang, D., Chen, M., 2014. J. Colloid Interface Sci. 433, 9–15.
Xu, Y., Chen, Y., Fu, W.F., 2018. Appl. Catal. B Environ. 236, 176–183.
Yan, K., Yang, Y., Okoth, O.K., Cheng, L., Zhang, J., 2016. Anal. Chem. 88, 6140–6144.
Yan, K., Zhu, Y., Ji, W., Chen, F., Zhang, J., 2018. Anal. Chem. 90, 9662–9666.
Yin, B.C., Wu, D., Ye, B.C., 2010. Anal. Chem. 82, 8272–8277.
Yu, Z., Schmaltz, R.M., Bozeman, T.C., Paul, R., Rishel, M.J., Tsosie, K.S., Hecht, S.M., 2013. J. Am. Chem. Soc. 135, 2883–2886.
Zang, Y., Lei, J., Hao, Q., Ju, H., 2016. Biosens. Bioelectron. 77, 557–564.
Zhou, J., Tian, G., Chen, Y., Shi, Y., Tian, C., Pan, K., Fu, H., 2014. Sci. Rep. 4, 4027.
Zhou, N., Yang, L., Hu, B., Song, Y., He, L., Chen, W., Zhang, Z., Liu, Z., Lu, S., 2018. Anal. Chem. 90, 13624–13631.
Zhu, H., Fan, G.C., Abdel-Halim, E.S., Zhang, J.R., Zhu, J.J., 2016. Biosens. Bioelectron. 77, 339–346.
Zhu, Y., Yan, K., Xu, Z., Wu, J., Zhang, J., 2019. Biosens. Bioelectron. 131, 79–87.